Statistical characteristics of raindrop size distribution during rainy seasons in Complicated Mountain Terrain

Wenqian Mao[1, 3,4], Wenyu Zhang[2,3,4], Menggang Kou[2]

1. College of Resources and Environmental Sciences, Gansu Agricultural University, Lanzhou 730070, China

2. School of Geoscience and Technology, Zhengzhou University, Zhengzhou, 450001, China

3. Key Laboratory for Cloud Physics, Chinese Academy of Meteorological Sciences, Beijing 100081, China

4. College of Atmospheric Sciences, Lanzhou University, Lanzhou, 730000, China

Correspondence to: Wenqian Mao (mdycmwq@163.com)

Abstract: In order to improve understanding of the characteristics of raindrop size distribution (DSD) over complex mountainous terrain, the differences in DSD over the southern slopes, northern slopes and interior of the Qilian Mountains were analyzed using six months of observations. For all rainfall events, the number concentrations of small and large raindrops in the interior and on the southern slopes were greater than on the northern slopes, but midsize raindrops were less. The DSD spectrum of the interior was more variable and differed significantly from that of the northern slopes. The differences in the normalized intercept parameters of the DSD for stratiform and convective rainfall were 8.3% and 10.4%, respectively, and those of the mass-weighted diameters were 10.0% and 23.4%, respectively, while the standard deviations of DSD parameters at interior sites were larger. The differences in the coefficient and exponent of the Z-R relationship were 2.5% and 10.7%, respectively, with an increasing value of the coefficient from the southern to the northern slopes for stratiform rainfall, but the opposite for convective rainfall. In addition, the DSD characteristics and Z-R relationships were more similar at the ipsilateral sites and had smaller differences between the southern slopes and interior of the mountains.

Keywords: *raindrop size distribution; complicated mountain terrain;* spatial variation

1 Introduction

Raindrop size distribution (DSD), the number of raindrops per drop size per unit volume, is an important parameter to statistically describe the microstructure of precipitation (Bringi et al., 2003; Ma et al., 2019a). The measurement of DSD can provide some fundamental information such as raindrop size (D), liquid water content (W), rain rate (R), radar reflectivity factor (Z) and so on, which has an essential contribution to improving quantitative precipitation estimation (QPE) using weather radar and satellite observations (Adirosi et al., 2018; Jash et al., 2019). The parameterization of DSD can obtain the distribution model parameters of DSD in different rain types, which is significant in advancing microphysics parameterization in numerical weather prediction (NWP) models (Wainwright et al., 2014; McFarquhar et al., 2015; Zhao et al., 2019). In addition, understanding the DSD is crucial in many applied fields concerning hydrology, agriculture, soil erosion and microwave communication (Rincon et al., 2002; Smith et al., 2009; Angulo-Martínez et al., 2015; Lim et al., 2015; Yang et al., 2016).

Numerous studies have been carried out on the statistical characteristics of DSD in different regions (Campos et al., 2006; Seela et al., 2017; Dolan et al., 2018; Protat et al., 2019; Loh et al., 2019; Jash et al., 2019). It has been shown that the number concentration and size of raindrops increase with rain rate and so the DSD becomes higher and wider. The characteristics in different rain types demonstrate that the mass-weighted mean diameter (i.e., D_m) and normalized intercept parameter (i.e., N_w) of convective rainfall are larger than those of stratiform rainfall. Furthermore, these studies also reveal that there are more differences in the characteristics of DSD. Dolan et al. (2018) divided global DSD characteristics into 6 types by using 12 datasets across three latitudes and found that the centralized regions and DSD parameters of the 6 types varied in location. The average number of raindrops in central Korea was usually greater than that in the southeast under three rainfall systems, especially drops in the 0.31–0.81mm diameter range (Loh et al., 2019). According to DSD measurements in the Tibetan Plateau region, eastern areas have a higher raindrop number concentration in the diameter range of 0.437–1.625 mm and greater variation indiameters than in central areas (Wang et al., 2020). Compared to eastern China and northern China, the DSD in southern China shows a higher number concentration of relatively small-sized drops (Zhang et al., 2019). Comparison of the Z-R relationship (defined as $Z=AR^b$) indicates that the coefficient decreases with increasing R in the southern Tibetan Plateau, which is opposite to the case in South China (Wu et al., 2017). For the DSD parameters of stratiform and convective rainfall, there are various changes between the lower and middle reaches of the Yangtze River (Fu et al., 2020).

As reported in the above studies, DSD characteristics vary significantly with factors such as geographical location, climatic region and rain types. Pu et al. (2020) analyzed the DSD characteristics of five sites in Nanjing city and found the N_w of DSD to be largest at site near industrial areas, but the D_m of DSD was largest at sites near the city's center. In other words, even at the urban scale, there are still differences in the microphysical characteristics reflected by the DSD, which is due to the influence of the surrounding environment. How, then, do the characteristics of DSD vary from location

to location over the complicated mountain terrain? Rao et al. (2006), by comparing the DSD parameters at different altitudes, suggested that the obvious variation in DSD with altitude is related to the processes of evaporation and breakup. Using aircraft observations, Geoffroy et al. (2014) concluded that the total concentration of raindrops decreased while the average drop size increased with decreasing altitude. But how large might the differences in DSD be at different altitudes in mountainous regions? And how significant might the effects be of these differences?

The Qilian Mountains, a series of marginal mountains in the northeastern part of the Tibetan Plateau, are a vitally important ecological protection barrier in the northwest arid areas of the region, that block the connection between deserts and wilderness (Figure 1a). The mountains form several inland rivers that are important water sources for the arid areas of the northwest and have therefore made a considerable contribution to regional economic development (Gou et al., 2005; Tian et al., 2014; Qin et al., 2016). In this study, we chose the Qilian Mountains as the research object and selected six sites with different backgrounds representing the southern slopes, northern slopes and interior of the mountains. To thoroughly investigate the discrepancies in this complex mountain terrain, the DSD characteristics and *Z-R* relationships were comprehensively analyzed according to different rain types based on continuous disdrometer observations in the rainy season. The primary goal was to obtain a deeper understanding and characteristic differences of DSD over the Qilian Mountains and improve the accuracy of QPE, which could then be used as a research foundation for developing cloud water resources in mountainous areas.

2   Data and method

2.1 Sites and instruments

The eastern and middle sections of the Qilian Mountains were chosen as the main study area, taking into account that several important inland rivers originate from these areas (Li et al., 2019). Six disdrometers were deployed on the southern slopes, northern slopes and interior (close to the ridge) of the Qilian Mountains, with three sites in the eastern section [called Taola (TL), Huangchengshuiguan (HS) and Liuba (LB), from south to north] and another three sites in the middle section [called Daladong (DLD), Boligou (BLG) and Shandan (SD), from south to north]. The background of the Qilian Mountains is shown on the satellite map in Figure 1a, and the six sites are marked on the topographical map, also in Figure 1b. The distances between the six sites are listed in Table 1. The sites in the south, north and interior are basically parallel to the orientation of the mountains, and the sections formed by the sites in the east and interior are basically perpendicular to it. On the basis of an historical weather review and rain gauge observations, the rainy season at the six sites is concentrated in May to October, with more precipitation in July, August and September.
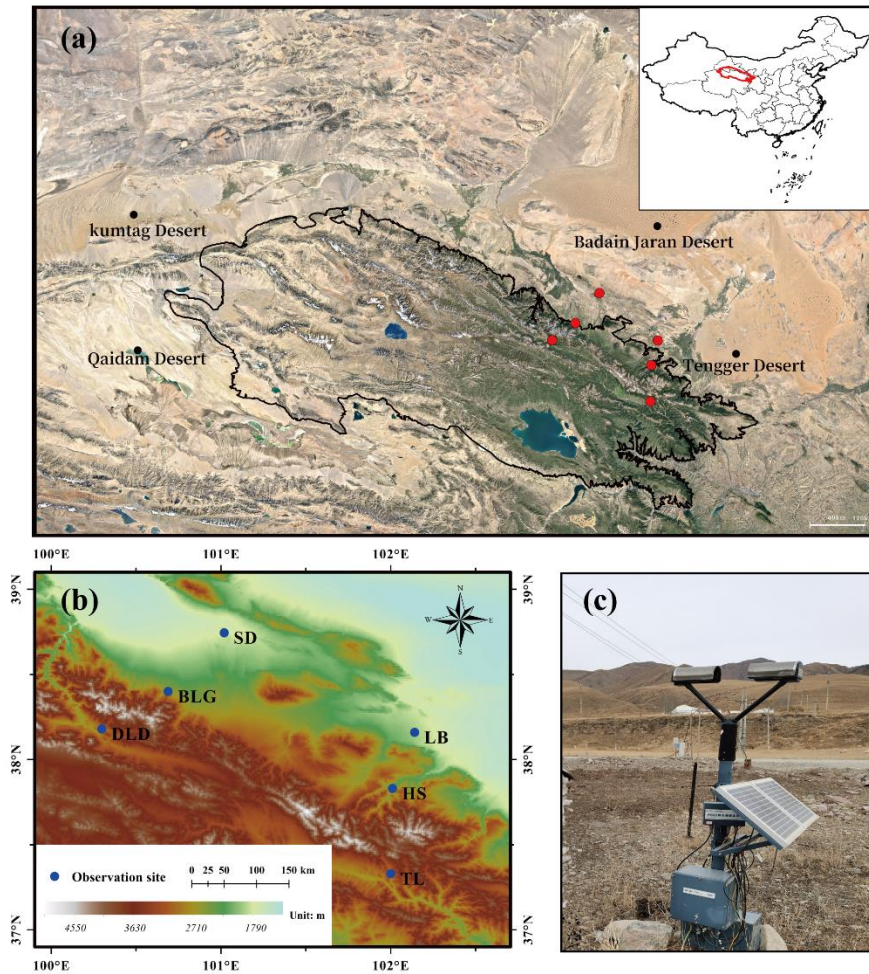
114
115 Figure 1. (a) Geographical overview of the Qian Mountains; (b) the disdrometer sites
116 (circles); (c) the observation device at TL site. Source: Google Earth © Google Earth
117 YEAR

118 Table 1. Site details (latitude, longitude, sea level height) and distances (km) between
119 pairs of sites.

Six sites	LB	HS	TL	SD	BLG	DLD
LB (38.16°N, 102.14°E, 1926m)	-	39.6	94.3	116.0	129.6	161.1
HS (37.83°N, 102.01°E, 2342m)	-	-	55.6	135.1	132.8	154.9
TL (37.33°N, 102.00°E, 2910m)	-	-	-	182.4	167.3	177.0
SD (38.80°N, 101.08°E, 1765m)	-	-	-	-	54.2	96.8
BLG (38.4°N, 100.69°E, 2455m)	-	-	-	-	-	43.3
DLD (38.18°N, 100.3°E, 2957m)	-	-	-	-	-	-

120 Thisstudy used an optical, laser-based device to measure the DSD, called a DSG4
121 disdrometer (Figure 1c), which meets the Functional Specification Requirements for
122 Disdrometer issued by the China Meteorological Administration. This disdrometer has
123 an HSC-OTT Parsivel2 sensor as the observation part, manufactured by OTT
124 Messtechnik (Germany) and Huatron (China). When raindrops pass through the
125 horizontal flat laser beam generated by the transmitting part of the instrument, it causes

signal attenuation in the laser observation area. The raindrop size is determined by the degree of signal attenuation and the falling speed is recorded by the transit time. The sampling time is 60s and the velocity and drop sizes are divided into 32 non-equally spaced bins, varying from 0.05 to 20.8 m s^{-1} for velocity and 0.062 to 24.5 mm for drop diameter.

2.2 Quality control of the data

It was necessary to quality control the data because of potential instrument error. Every minute of DSD data collected by the six DSG4 disdrometers from May to October 2020 was carefully processed. Specifically, the following criteria were employed in choosing data for analysis(Jaffrain et al., 2011; Guyot et al., 2019; Pu et al., 2020): (1) the first two size bins were ignored because of low signal-to-noise ratio; (2) samples with 1-min total of raindrop number less than 10, or a rain rate at the moment of discontinuous observation less than 0.1 mmh^{-1} were regarded as noise; (3) raindrops with diameters more than 8 mm were eliminated; (4) raindrops with a falling terminal velocity $V(D_i)$ that deviated from the empirical terminal velocity $V_{emp}(D_i)$ by more than 40% were removed (Kruger and Krajewski, 2002); and (5) samples with less than five bins after the correction of falling terminal velocity were deleted because their DSDs could not be determined with too few bins. The fourth criterion can be expressed by the formula:

$$\left|V(D_i) - V_{emp}(D_i)\right| < 0.4V_{emp}(D_i) \tag{1}$$

where $V_{emp}(D_i) = 9.65 - 10.3\exp(-0.6D_i)$ (D_i is the mean volume-equivalent diameter of the ith size category), as derived from the formula given in Atlas et al. (1973).

After data quality control, the sample statistics of key steps are shown in Table 2. The number of 1-min DSD spectra selected from the six sites (LB, HS, TL, SD, BLG, DLD) after data quality control covering the rainy season (May–October) in the Qilian Mountains region in 2020 were 11103, 17619, 14814, 10736, 18861 and 13230, respectively, which accounted for 87.9%, 85.8%, 84.5%, 91.2%, 80.6% and 86.5% of the total number of samples.

Table 2. Sample statistics of data quality control at six sites

Samples	LB	HS	TL	SD	BLG	DLD
Total minutes (min)	12625	20536	17526	11770	23401	15289
Total minutes without noise (min)	12602	20509	17494	11756	23371	15267
After quality control (min)	11103	17619	14814	10736	18861	13230
Available rain minutes (%)	87.9%	85.8%	84.5%	91.2%	80.6%	86.5%

2.3 Integral parameters of rainfall

The basic observations obtained by the disdrometer were the counts of raindrops at each diameter and velocity. Also, the diameters given by the disdrometers were the mid value of two adjacent bins, which we take as the corresponding endpoint bin values. The velocities were the weighted average velocity class over the corresponding

disdrometer. The raindrop number concentration $N(D_i)$ (m^{-3} mm^{-1}) in the ith size bin per unit volume per unit size interval for diameter was calculated by the following equation:

$$N(D_i) = \sum_{i.j=1}^{32} \frac{n_{i,j}}{A \cdot \Delta t \cdot V_j \cdot \Delta D_i} \tag{2}$$

where $n_{i,j}$ denotes the counts of raindrops measured by the disdrometer within size bin i and velocity bin j during the sampling time Δt; A and Δt are the sampling area (0.0054 m^2) and sampling time (60 s), respectively; V_j (m s^{-1}) is the mid-value falling speed for velocity bin j; and ΔD_i is the diameter spread for the ith diameter bin.

Some integral rainfall parameters, such as the total number concentration N_t (m^{-3}), rain rate R (mm h^{-1}), radar reflectivity factor Z (mm^6 m^{-3}) and liquid water content W (g cm^{-3}), can be derived by the following equations:

$$N_t = \sum_{i=1}^{32} N(D_i)\Delta D \tag{3}$$

$$R = \frac{6\pi}{10^4 \rho_w} \sum_{i=1}^{32} V(D_i) D_i^3 N(D_i)\Delta D_j \tag{4}$$

$$Z = \sum_{i=1}^{32} N(D_i)D_i^6 \Delta D_i \tag{5}$$

$$W = \frac{\pi \rho_w}{6 \times 10^3} \sum_{i=1}^{32} D_i^3 N(D_i)\Delta D_i \tag{6}$$

where ρ_w is the water density (1.0 gcm^{-3}); and $V(D_i)$ is the falling speed from the disdrometer. In this study, when calculating the rain rate we use $V_{emp}(D_i)$ to replace $V(D_i)$ because of measurement error, particularly at larger bins and faster falling speeds.

The characteristics of DSD can be described by a three-parameter gamma distribution in the form introduced by Ulbrich (1983). Also, it has better fitting capability than the M-P distribution on the broader variation of DSD fluctuations, including the middle rain drops, especially on small and large rain scales. The three-parameter gamma distribution can be expressed by the following formula:

$$N(D) = N_0 D^\mu \exp(-\Lambda D) \tag{7}$$

where $N(D)$ is the raindrop number concentration; D is the raindrop bins with unit mm; and N_0, μ and Λ are the intercept, shape and slope parameter from the three parameters of the gamma model, which can be derived from gamma moments or the least-squares method, respectively. When $\mu=0$, it degenerates into the M-P DSD model.

Although, the gamma distribution is commonly accepted, the normalized gamma distribution has also been widely adopted with its independent parameters and clear physical meaning as follows (Dolan et al., 2018; Ma et al., 2019):

$$N(D) = \frac{3}{128} N_w \left[\frac{(4+\mu)^{(4+\mu)}}{\Gamma(4+\mu)} \right] \left(\frac{D}{D_m} \right)^\mu \exp\left(\frac{-(4+\mu)D}{D_m} \right) \tag{8}$$

194 where μ is the shape parameter, which is in dimensionless; D_m (mm) is the mass-
195 weighted mean diameter, and N_w (m^{-3} mm^{-1}) is the normalized intercept parameter
196 computed from D_m. The form is as follows:

197
$$D_m = \frac{\sum_{i=1}^{32} N(D_i)D_i^4 \Delta D_i}{\sum_{i=1}^{32} N(D_i)D_i^3 \Delta D_i} \tag{9}$$

198
$$N_w = \frac{4^4}{\pi \rho_w}\left(\frac{10^3 W}{D_m^4}\right) \tag{10}$$

199 **3   DSD parameter characteristics**

200 **3.1 Characteristics of DSD**

201   Figure 2a shows the mean DSDs for the six sites during the rainy season in the
202 Qilian Mountains. The maximum concentration of raindrops was around 0.562 mm in
203 diameter and the maximum number concentration values of sites were order as follows:
204 BLG>TL>DLD>HS>SD>LB. As the diameter increased, the number concentration
205 decreased   and   the   concentration   values   followed   the   order
206 LB>SD>DLD>TL>BLG>HS at around 2 mm in diameter. When the diameter was
207 larger than 4 mm, the concentration at TL, BLG and HS was relatively high. In this
208 study, the data were roughly divided into small raindrops (less than 1 mm in diameter),
209 midsize raindrops (1–3 mm) and large raindrops (greater than 3 mm) to easily describe
210 the difference in DSDs (Ma et al., 2019b; Pu et al., 2020). To highlight the DSD
211 differences caused by the background environment, Figure 2b shows the mean DSDs
212 normalized by the N_w and D_m results for the sites. Compared with Figure 2a, the
213 raindrop characteristics were more consistent across sizes, while the differences
214 between the sites were more pronounced, especially in the midsize and large raindrops,
215 which truly reflected the DSD differences caused by the location. Combining the
216 characteristics of the geographical environment of the six sites, we can analyze some
217 differences in DSD characteristics in the Qilian Mountains. For small raindrops, the
218 number concentrations at interior and southern-slope sites were greater than at northern-
219 slope sites; for midsize raindrops, the number concentrations decreased sequentially at
220 the northern-slope, southern-slope and interior sites; and for large raindrops, the number
221 concentrations at the interior sites were larger. In addition, the number concentrations
222 of raindrops in the middle section of this the mountainous area were slightly greater
223 than those in the eastern section.
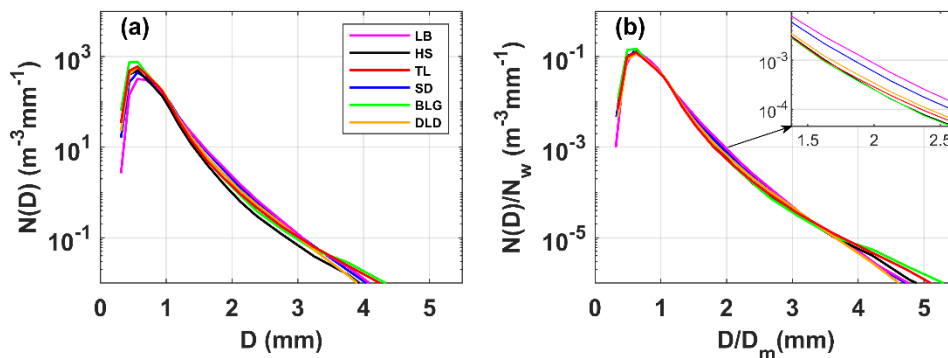
224

225 Figure 2. The (a) mean and (b) normalized mean DSDs at six sites in the Qilian
226 Mountains region in the rainy season

3.2 Distribution of DSD parameters

228   In order to study the differences in DSDs, we selected six integral rainfall
229 parameters for discussion—namely, the normalized intercept parameter (N_w), mass-
230 weighted mean diameter (D_m), shape parameter (μ), total number concentration (N_t),
231 rain rate (R) and radar reflectivity factor (Z). Figure 3 and Table 3 show the distributions
232 and statistics of these six DSD parameters (the distribution of each was normalized
233 using the uniform method). On average, D_m was more concentrated on smaller values
234 at HS and BLG, which showed smaller mean values than TL and DLD but significantly
235 more values greater than 1 mm at LB and SD; $\log_{10}N_w$ was more centralized on larger
236 values at TL and DLD, with relatively smaller values at LB and SD; and the distribution
237 patterns for μ and $\log_{10}N_t$ were similar to those for $\log_{10}N_w$. The density curves of R and
238 Z were similar, but there were differences among the six sites, which are analyzed in
239 detail later in the paper. It is noteworthy that the frequency of samples with R around
240 0.6–1.0 mm h^{-1} was highest, and samples with R less than 1mm h^{-1} accounted for more
241 than half of the total rainfall.
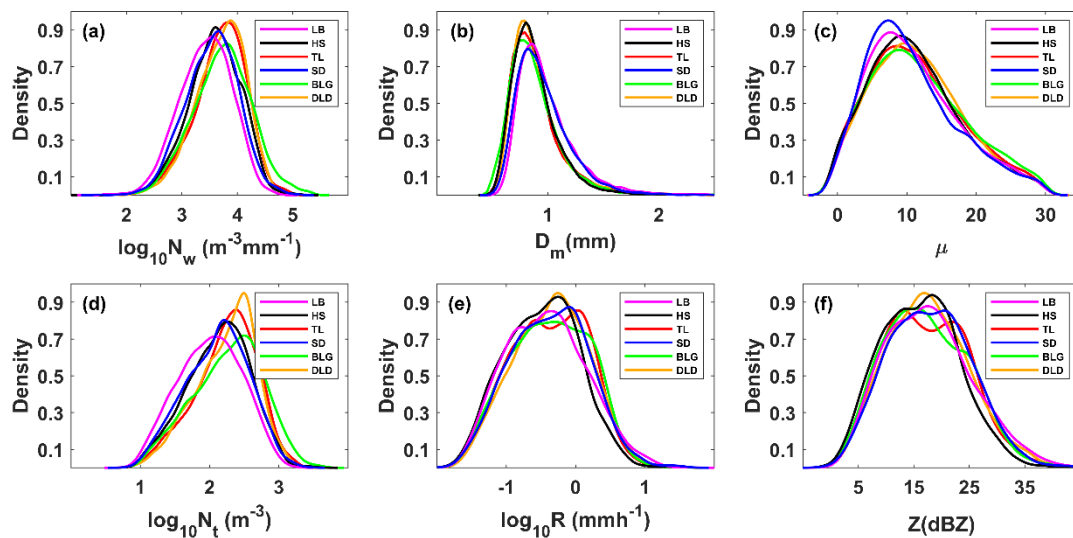
242
243 Figure 3. Probability density distribution of integral DSD parameters at six sites (LB,
244 HS, TL, SD, BLG, DLD): (a) normalized intercept parameter $\log_{10}N_w$ (m^{-3}mm^{-1}); (b)
245 mass-weighted mean diameter D_m (mm); (c) shape parameter μ; (d) total number
246 concentration $\log_{10}N_t$ (m^{-3}); (e) rain rate R (mm h^{-1}); (f) radar reflectivity factor Z (dBZ)

247 Table 3. Statistical of several integral DSD parameters for all observations at six sites
248 (LB, HS, TL, SD, BLG, DLD).

Sites	$\log_{10}N_w$ (m^{-3}mm^{-1})			D_m (mm)			μ			$\log_{10}N_t$ (m^{-3})			R (mm h^{-1})			Z dBZ		
	ME	SD	SK	ME	SD	SK	ME	SD	SK	ME	SD	SK	ME	SD	SK	ME	SD	SK
LB	3.43	0.47	-0.25	0.99	0.29	2.68	10.92	6.63	0.61	2.01	0.46	-0.07	0.94	1.90	0.23	17.79	7.82	0.44
HS	3.59	0.48	-0.29	0.89	0.25	3.35	11.12	6.64	0.53	2.13	0.45	-0.22	0.69	1.60	0.05	16.24	7.08	0.34
TL	3.69	0.48	-0.55	0.90	0.29	4.49	11.37	6.84	0.48	2.23	0.44	-0.43	0.89	1.48	-0.05	17.47	7.55	0.35

SD	3.54	0.48	-0.17	0.96	0.26	2.12	10.62	6.61	0.71	2.11	0.46	-0.17	0.97	2.01	0.06	17.95	7.47	0.28
BLG	3.72	0.54	-0.15	0.89	0.29	5.17	11.71	7.06	0.46	2.26	0.50	-0.25	0.94	2.13	-0.04	17.34	7.66	0.41
DLD	3.69	0.45	-0.50	0.90	0.25	2.66	11.52	6.66	0.43	2.24	0.43	-0.46	0.95	1.62	-0.01	17.70	7.43	0.37

249   Note: ME is mean; SD is standard deviation; SK is skewness.

3.3 DSD characteristics in different rain rate classes

251   To further understand the characteristics of DSDs at the six sites, the samples were divided into six classes according to the associated rain rates (R): C1, $R<0.5$; C2, $0.5 \leq R < 2$; C3, $2 \leq R < 4$; C4, $4 \leq R < 6$; C5, $6 \leq R < 10$; C6, $R \geq 10$ mm h^{-1}. This classification was based on two considerations: firstly, the number of observation samples in different rainfall rates roughly conformed to a normal distribution; and secondly, the mean maximum diameter interval of different rainfall rates gradually increased (Li et al., 2019). Of course, other classification studies were referenced and the fact that the rain rate in this area is smaller than that in southern China was taken into account (Ma et al., 2019b; Zeng et al., 2021). Figure 4 shows the mean DSDs at each rainfall rate class for the six sites. Table 4 lists the number of samples and statistical values of the DSD parameters for the six classes. Clearly, as the rainfall rate increased, the number concentration of almost all raindrop sizes and the width of DSD shapes increased, and thus the tail of the DSD shape moved gradually towards a larger diameter, similar to previous findings, such as those of Ma et al. (2019b) and Pu et al. (2020). Taking a number concentration of 0.01 m^{-3}mm^{-1}, the mean maximum diameter of DSD in each class was ordered as follows:: 2.3–2.5, 3.2–3.4, 3.9–4.5, 4.3–5.0, 5.0–5.6 and 6.0–7.0 mm (the sixth-class diameter range is not fully shown in the figure). In class C1, the number concentrations were relatively similar at different sites; starting from class C2, the differences in number concentration increased when the diameter was greater than 2 mm for the six sites; and the differences of in number concentration were gradually reflected in each raindrop size bin as the rainfall rate class increased. Observationally, the DSDs of BLG, HS and TL had larger number concentrations in different rainfall rate classes, and the DSD parameters and standard deviations (SDs) were larger, especially for BLG.

275   Table 4. Statistics of several integral DSD parameters for six rain rate classes at six sites.

Class	Sites	Samples	$\log_{10}N_w$ (m^{-3}mm^{-1})		D_m (mm)		μ		$\log_{10}N_t$ (m^{-3})		R (mm h^{-1})		Z dBZ	
			ME	SD	ME	SD	ME	SD	ME	SD	ME	SD	ME	SD
C1(<0.5 mm h^{-1})	LB	6520	3.25	0.41	0.88	0.18	12.36	7.09	1.74	0.34	0.20	0.13	12.68	4.52
	HS	10753	3.43	0.44	0.81	0.17	12.01	7.03	1.89	0.37	0.20	0.13	11.90	4.54
	TL	7858	3.52	0.44	0.79	0.16	12.91	7.12	1.96	0.37	0.20	0.13	11.78	4.16
	SD	5772	3.34	0.43	0.85	0.18	11.72	6.99	1.82	0.36	0.20	0.13	12.51	4.40
	BLG	10073	3.50	0.48	0.79	0.17	12.94	7.28	1.94	0.40	0.20	0.13	11.73	4.26
	DLD	6891	3.51	0.43	0.79	0.15	13.04	6.92	1.96	0.36	0.21	0.13	12.14	4.15
C2(0.5~2 mm h^{-1})	LB	3318	3.66	0.41	1.06	0.24	9.93	5.75	2.30	0.28	1.00	0.41	22.55	3.27
	HS	5700	3.82	0.39	0.97	0.21	10.21	5.88	2.44	0.26	0.96	0.37	21.67	3.09
	TL	5368	3.87	0.42	0.98	0.23	10.35	6.15	2.49	0.26	1.07	0.41	22.18	3.33

	SD	3778	3.73	0.41	1.03	0.23	9.94	6.14	2.36	0.28	1.02	0.40	22.40	3.15
	BLG	6411	3.97	0.47	0.94	0.25	11.24	6.72	2.56	0.30	1.07	0.43	21.69	3.69
	DLD	4778	3.88	0.37	0.95	0.20	10.91	6.02	2.47	0.24	1.01	0.40	21.60	3.19
C3(2~4 mm h^{-1})	LB	782	3.71	0.47	1.31	0.37	7.33	4.28	2.52	0.29	2.77	0.56	29.54	2.87
	HS	884	3.96	0.50	1.16	0.34	8.42	5.22	2.73	0.27	2.76	0.54	28.33	3.06
	TL	1232	4.00	0.47	1.13	0.33	8.70	5.93	2.75	0.23	2.68	0.53	28.07	3.16
	SD	812	3.89	0.44	1.19	0.27	8.57	5.53	2.63	0.26	2.71	0.53	28.41	2.68
	BLG	1865	4.05	0.49	1.11	0.30	8.62	5.75	2.81	0.25	2.70	0.53	27.99	3.29
	DLD	1111	3.91	0.44	1.18	0.29	7.81	5.45	2.70	0.23	2.74	0.54	28.73	3.09
C4(4~6 mm h^{-1})	LB	229	3.80	0.47	1.41	0.40	7.33	3.94	2.65	0.31	4.76	0.57	32.69	2.63
	HS	191	4.03	0.54	1.28	0.47	7.54	4.42	2.86	0.27	4.80	0.56	31.70	3.34
	TL	213	3.84	0.56	1.41	0.51	6.23	4.64	2.77	0.28	4.77	0.54	32.82	3.54
	SD	187	4.03	0.41	1.24	0.27	8.35	5.02	2.80	0.22	4.76	0.54	31.32	2.52
	BLG	321	3.99	0.66	1.33	0.53	7.97	6.10	2.93	0.27	4.78	0.54	32.44	4.40
	DLD	270	3.92	0.53	1.35	0.47	6.50	4.80	2.83	0.25	4.83	0.56	32.55	3.47
C5(6~10 mm h^{-1})	LB	167	3.81	0.46	1.55	0.44	6.46	3.38	2.72	0.27	7.66	1.22	35.74	2.85
	HS	49	3.69	0.74	1.70	0.68	6.89	4.82	2.75	0.38	7.42	1.09	36.14	4.29
	TL	103	3.57	0.62	1.78	0.66	5.20	4.62	2.71	0.32	7.32	1.02	37.03	3.76
	SD	128	3.96	0.39	1.42	0.35	7.10	3.96	2.82	0.21	7.68	1.17	34.76	2.42
	BLG	138	3.97	0.76	1.51	0.80	8.34	6.35	2.99	0.27	7.37	1.02	35.09	4.96
	DLD	122	3.90	0.46	1.46	0.34	6.13	4.20	2.86	0.26	7.29	1.11	35.32	2.88
C6(>10 mm h^{-1})	LB	87	3.85	0.44	1.73	0.53	5.08	3.05	2.87	0.32	14.81	7.57	39.58	3.57
	HS	42	3.60	0.65	2.19	0.92	6.74	5.27	3.00	0.28	21.69	9.91	42.93	6.11
	TL	40	3.16	0.69	2.69	1.19	4.34	5.20	2.74	0.32	18.25	9.69	44.70	5.41
	SD	59	3.66	0.29	2.04	0.46	3.30	2.48	2.91	0.16	21.07	8.34	42.85	4.10
	BLG	53	3.38	0.93	2.58	1.52	5.58	6.19	3.00	0.37	21.95	9.05	44.08	7.50
	DLD	58	3.82	0.47	1.80	0.46	6.64	4.12	2.84	0.28	16.58	7.21	40.13	3.53
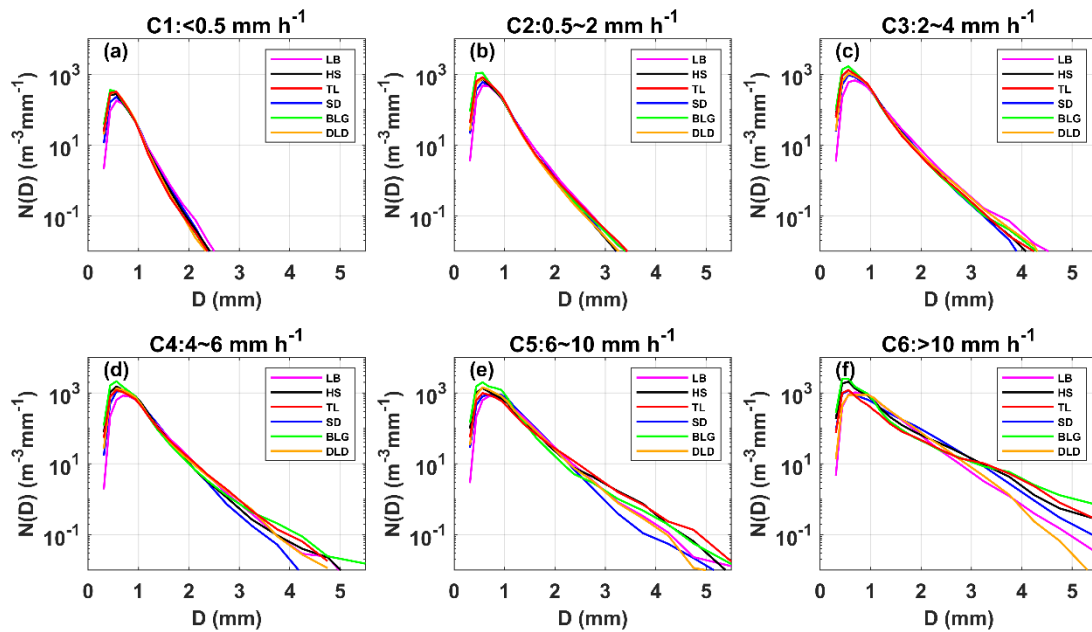
276

277   Figure 4. Distribution of mean measured DSD for different rain rate classes at six sites.

278   Figgure 5 shows box-and-whisker plots of the normalized intercept parameter
279    $\log_{10}N_w$ and mass-weighted mean diameter D_m for six sites in each rain rate class. The
280   middle line in the box indicates the median. The left and right lines indicate the 25th and
281   75th percentiles. The left and right ends of whiskers indicate the most extreme data
282   points between the 5th and 95th percentiles, except outliers. The median D_m gradually
283   increased with a larger value range as the rain rate class increased, particularly for HS
284   and BLG in class C5 and C6. The median $\log_{10}N_w$ increased in class C1 to C3 and then
285   tended to decrease in class C5 to C6, for which the reduction was obvious at sites with
286   a larger value range, such as HS and BLG. Ma et al. (2019b) also obtained similar
287   conclusions about D_m and $\log_{10}N_w$. The indication was that the increase in rain rate was
288   mainly due to the growth in raindrop size. Also, the change in number concentration
289   may have been caused by the imbalance between the loss of number concentration at
290   small raindrop size and the addition at large raindrop sizes, which in a sense implies a
291   relationship between the collision–coalescence and break–up of raindrops. It is worth
292   noting that the microphysical processes were quite different among the sites, being
293   greatly influenced by the surrounding environment. Because HS and BLG were located
294   in the interior of the mountains and close to the ridge, their dynamics and
295   thermodynamics as well underlying surfaces were thus different from those of other
296   sites.

297
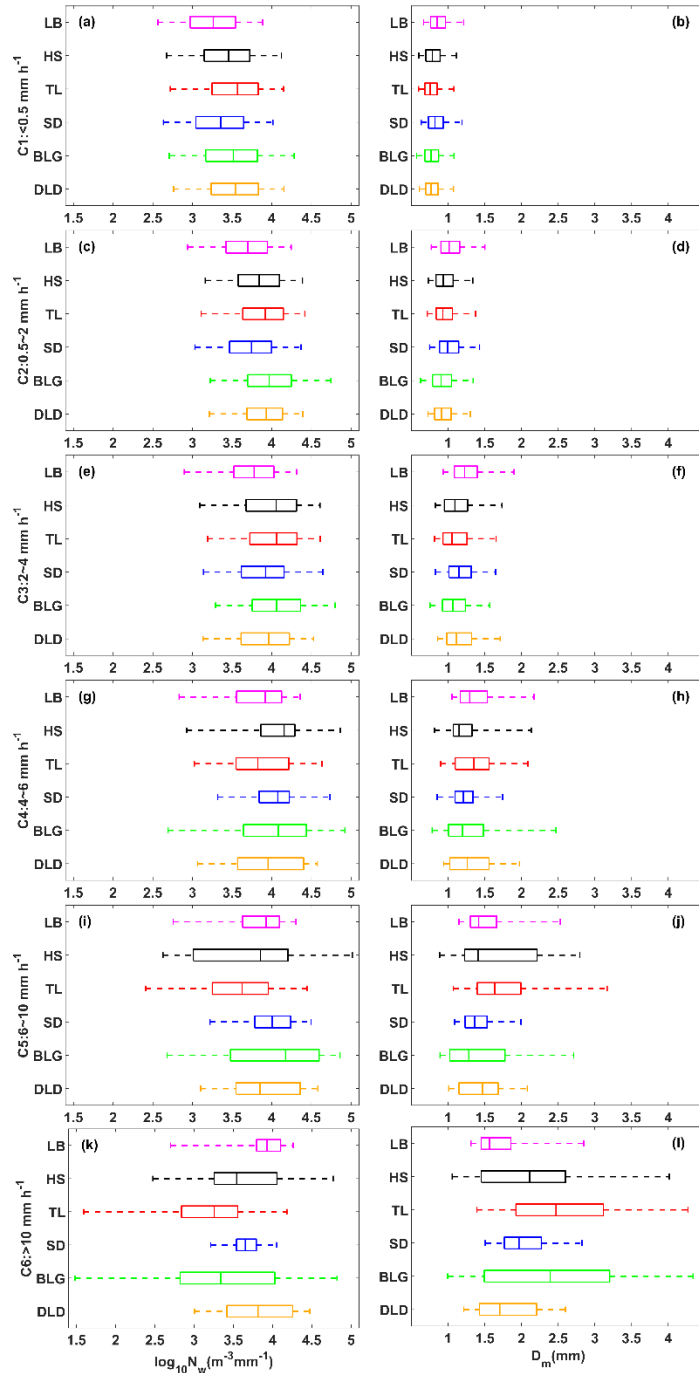
Figure 5. Variation of the normalized intercept parameter $\log_{10}N_w$ (a) and the mass-weighted mean diameter D_m (b) for different rain rate classes at six sites. The three lines in the boxes are the 25th, 50th and 75th percentiles, from left to right, respectively. The whiskers at the left and right ends are the 5th and 95th percentiles, respectively. The colors represent the six sites as in other figures.

Figure 6 displays the contribution of different rain rate classes to the total rainfall at different sites. It is clear that C2 contributed the most to the total rainfall of all sites, followed by C3, and the sum of the two classes' contribution could reach 60% of the total rainfall. Compared with the interior and southern-slope sites, C2 and C3 contributed slightly less to sites LB and SD (i.e., the northern slopes), while C5 and C6

308   contributed relatively more to sites LB and SD, indicating that there is a greater
309   probability of heavy precipitation events on the northern slopes. The DSD parameters
310   in Table 3 provide a more detailed representation of the rainfall differences between the
311   three geographical sections of the Qilian Mountains, i.e., the interior, southern slopes
312   and northern slopes. Meanwhile, it also reflects the characteristics of rainfall in the
313   eastern and interior sections, such as the eastern section had larger Z and D_m and smaller
314   $\log_{10}N_w$ and $\log_{10}N_t$ compared to the interior. It is possible that there is a certain spatial
315   connection between precipitation at the sites, related to factors such as the source of
316   precipitation vapor, weather system and so on.
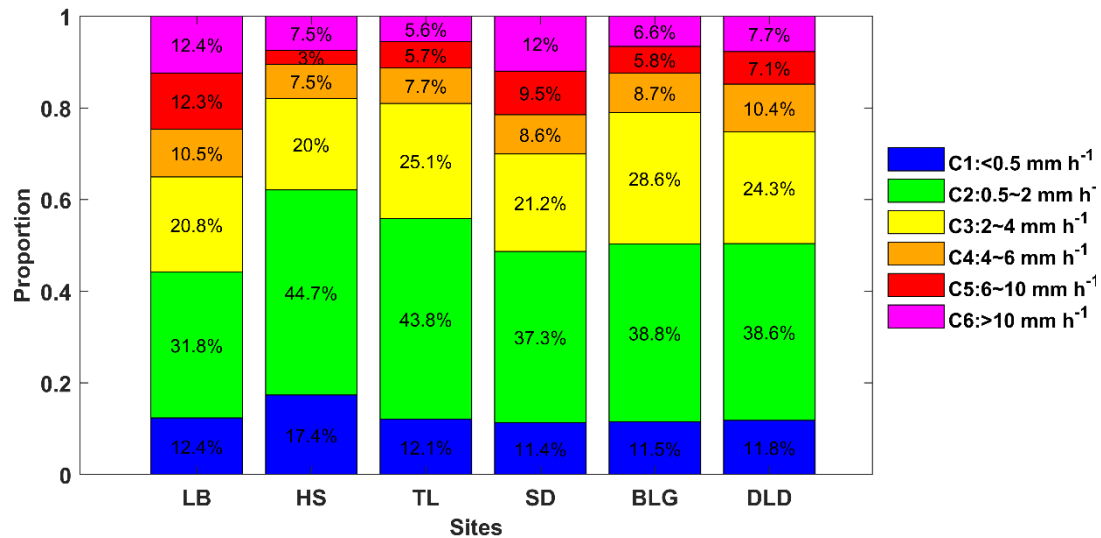
317
318   Figure 6. Proportion of rainfall with different rain rate classes to rain amount at six sites.

319   **3.4 DSD properties for different rain types**

320   Previous studies on DSD have shown that there are significant differences in the
321   DSD of convective and stratiform rainfall in the same climatic region, which has a
322   substantial impact on the parameterization of NWP and remote sensing observations
323   (Bringi et al., 2003; Penide et al., 2013). Due to the different physical mechanisms of
324   convective and stratiform rainfall, it is possible to discuss the differences in
325   microphysical structures for rainfall types through their DSD. Studies have employed
326   many different classification methods for rainfall types; example, Testud et al. (2001)
327   used the rain rate; Chen et al. (2013) combined the rain rate and its SD; and the findings
328   of Das et al. (2018) were based on the rain rate and radar reflectivity factor. Among
329   these, the method of Chen et al. (2013) has commonly been used to establish samples
330   of convective and stratiform rainfall, , but mainly in semi-humid or humid regions with
331   relatively high rain rate and rainfall. However, the Qilian Mountains are located in the
332   semi-arid regions of China and far from the sea, where the average rainfall rain and
333   rainfall are quite different from in semi-humid regions. Therefore, this paper proposes
334   a new classification method for precipitation applicable to the arid and semi-arid
335   regions of Northwest China based on the classification ideas of Chen et al. (2013) and
336   Das et al. (2018).
337   Firstly, the sequences of DSD with continuous 1-min samples more than 10 min

338 are determined, and R_t is defined as the rain rate at time t. In the first case, the R of
339 samples from R_{t-5} to R_{t+5} are all less than 5 mm h^{-1} and their SD is less than 1.5 mm
340 h^{-1}; in the second case, the R of samples from R_{t-5} to R_{t+5} are greater than or equal to 5
341 mm h^{-1} with more than nine samples and their SD is greater than 1.5 mm h^{-1}; and in
342 the third case, the situation is the same as the second case but their SD is less 1.5 mm
343 h^{-1}. Secondly, samples satisfying $Z<20$ and $W<0.08$ in the second case are removed
344 (Thurai et al., 2016; Das et al., 2018). And then, samples with R_t greater than or equal
345 to 5 mm h^{-1} in the second case are regarded as convective rainfall and samples with R_t
346 less than 5 mm h^{-1} in the second case are regarded as transitional rainfall (the rainfall
347 stage in which convective precipitation develops and declines). Samples in the first case
348 are regarded as stratiform rainfall. Through experiments, the third case does not exist.
349 The $\log_{10}N_w$ and D_m of different rainfall types were different, which were taken as
350 the main research objects. Figure 7 shows the variation of $\log_{10}N_w$ with D_m at different
351 sites. The blue, red and yellow scatter points represent stratiform, convective and
352 transitional rainfall, respectively. Obviously, there are fairly clear boundaries between
353 the scatter points for the different precipitation type events, and the same dividing line
354 can be used to distinguish between the different rainfall types at different sites. The
355 black solid lines were drawn based on visual examination of the data with a slope of
356 approximately −1.60 and intercept of 6.008 to represent the split between stratiform,
357 transitional and convective rainfall in all subplots. The black dashed line can distinguish
358 transitional rainfall (transitional and stratiform rainfall have an overlap area) with a
359 slope of approximately −3.338 and intercept of 6.847. Note that the dividing line
360 between stratiform and convective rainfall has the same slope as that obtained by Bringi
361 et al. (2003) (solid green line with a slope of −1.6 and intercept of 6.3), who fitted
362 composite results based on disdrometer data and from radar retrievals covering many
363 climate conditions from near the equator to plateau. The $\log_{10}N_w$ and D_m from the
364 figures for stratiform, convective and transitional rainfall are respectively concentrated
365 in the ranges of 3.1–3.9 m^{-3}mm^{-1}, 0.75–1.1 mm; 3.8–4.2 m^{-3}mm^{-1}, 1.4–1.6 mm; 3.6–
366 4.0 m^{-3}mm^{-1}, 1.05–1.2 mm. Compared to the maritime-like cluster and continental-like
367 cluster of convective rainfall proposed by Bringi et al. (2003), the convective events in
368 the Qilian Mountains are more consistent with the continental-like cluster (the gray
369 rectangle with smaller $\log_{10}N_w$ and larger D_m in Fig. 7). There are isolated convective
370 events in the maritime-like cluster, but it is difficult to have more events from the trend
371 between $\log_{10}N_w$ and D_m. This is also consistent with the features of the geographical
372 location of the Qilian Mountains.
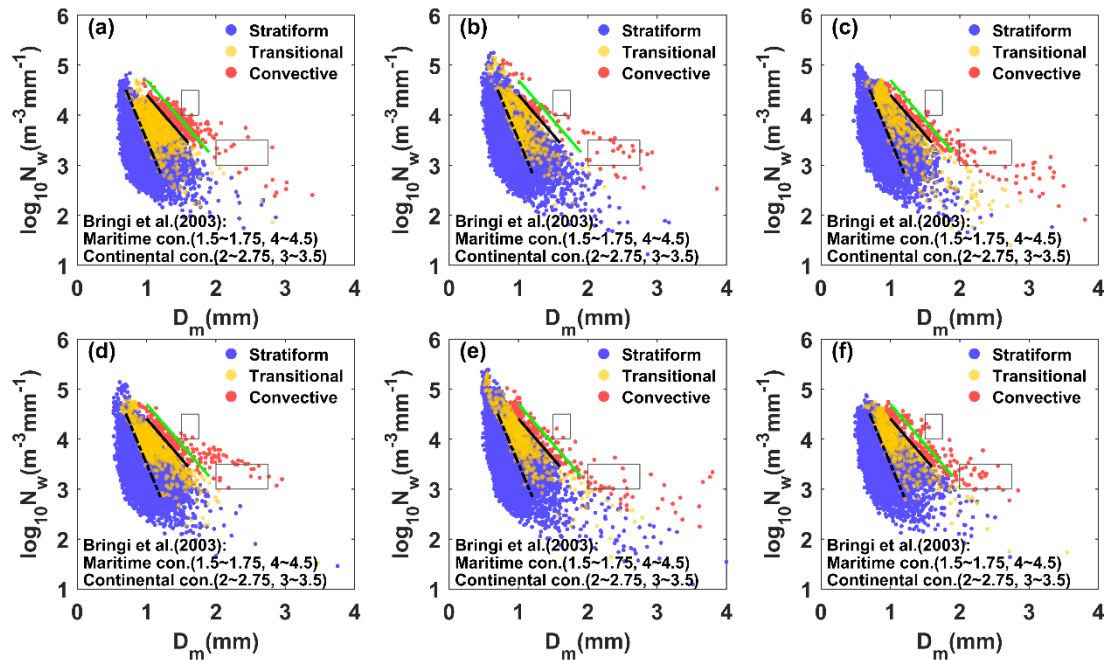
Figure 7. Scatter plot of $\log_{10}N_w$ versus D_m for different rain types at (a) LB, (b) HS, (c) TL, (d)SD, (e)BLG, and (f)DLD. The stratiform cases, convective cases and transitional cases are represented by blue, red and yellow scatter points,, respectively. The black dashed lines are the $\log_{10}N_w$–D_m relationship for stratiform versus convective cases and stratiform versus transitional case.

Figure 8 shows the mean DSDs for stratiform, convective and transitional rainfall at the six sites. The range of number concentrations and corresponding raindrop diameters for the three types were significantly different, matching the basic characteristics of DSD. The mean DSDs of stratiform rainfall differed slightly among the sites; convective rainfall had big differences at among the sites; and transitional rainfall presented more differences beginning at larger than 2.2 mm in diameter, which were the expected results. Stratiform rainfall usually has a large horizontal extent and an homogeneous cloud distribution, which makes the DSD characteristics basically the same under the influence of the same cloud system in mountainous areas. However, convective rainfall is related to local thermal and dynamical factors, which could lead to differences in DSD at different sites when considering the complex topography and diverse underlying surfaces in mountainous areas. For example, for convective rainfall, there was a significant increase in the number concentration of raindrops larger than 2.2 mm in diameter at BLG, HS and TL, indicating that these sites are conducive to the development of convective precipitation. Also, the number concentration of small raindrops at BLG and HS were higher than at TL (the southern slope), which may be due to the higher altitude of the interior sites reducing the falling distance of raindrops after exiting the cloud and decreasing the impact of collision on the raindrop evolution. In other words, even for the same rainfall type, the microphysics of rainfall at different sites is still different, depending on the topography and position of the observation point relative to the cloud base.
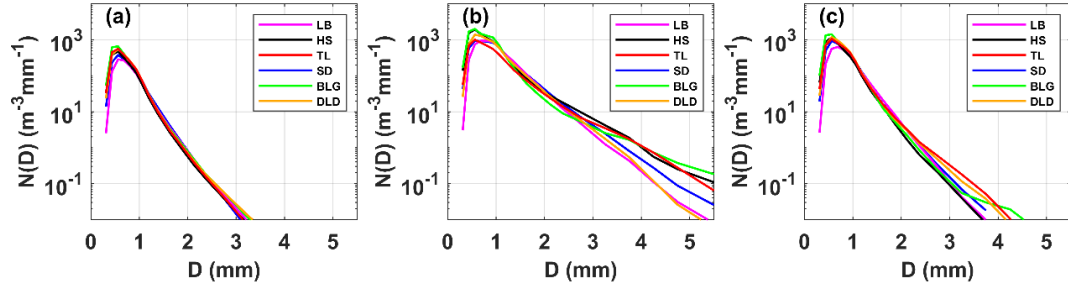
400

401 Figure 8. Distribution of mean measured DSD for (a) stratiform rainfall, (b) convective
402 rainfall and (c) transitional rainfall at six sites.

403   Figure 9 shows box-and-whisker plots of $\log_{10}N_w$ and D_m for different rain types.
404 The $\log_{10}N_w$ and D_m of stratiform rainfall were smaller than those of convective rainfall
405 but larger than those of transitional rainfall. Sites with a large $\log_{10}N_w$ value range had
406 larger value ranges for D_m; and sites with a large median $\log_{10}N_w$ had a smaller median
407 D_m, especially at sites HS and BLG for convective rainfall. Based on the mean values
408 of the six sites in Table 5, the DSD characteristics in the Qilian Mountains consist of a
409 larger N_w and smaller D_m due to the melting of tiny, compact graupel, and rimed ice
410 particles (relative to large, low-density snowflakes). Compared with transitional rainfall,
411 the D_m of convective rainfall was obviously larger, indicating that the increase in rain
412 rate in this area is mainly due to the growth in raindrop size. Moreover, on the northern
413 slopes one should consider the increase in number concentration, because the $\log_{10}N_w$
414 of convective rainfall also increased. Note that the number of convective samples on
415 the northern slopes was higher than that of other sites, which corresponds to the
416 speculation regarding the contribution of different rain rate classes. On average, for
417 stratiform rainfall, the dispersion degree of $\log_{10}N_w$ and D_m at different sites was 8.3%
418 and 10.0%, respectively; and for convective rainfall it was 10.4% and 23.4%. The SDs
419 of DSD parameters at sites HS and BLG were relatively large.

420 Table 5 Statistics of several integral DSD parameters for six sites with stratiform rainfall,
421 convective rainfall and transitional rainfall

Type	Sites	No. samples	$\log_{10}N_w$ (m^{-3}mm^{-1})		D_m (mm)		μ		$\log_{10}N_t$ (m^{-3})		R (mm h^{-1})		Z dBZ	
			ME	SD	ME	SD	ME	SD	ME	SD	ME	SD	ME	SD
S	LB	7123	3.42	0.42	0.96	0.21	11.48	7.98	1.98	0.38	0.54	0.60	16.93	5.93
	HS	12694	3.60	0.44	0.88	0.21	11.24	7.89	2.14	0.40	0.54	0.58	16.17	6.06
	TL	10091	3.71	0.43	0.87	0.20	11.90	8.01	2.23	0.39	0.65	0.67	16.85	6.15
	SD	7175	3.51	0.44	0.95	0.22	11.15	8.03	2.07	0.39	0.62	0.64	17.36	6.10
	BLG	12467	3.72	0.49	0.88	0.23	12.24	8.50	2.25	0.44	0.70	0.74	17.11	6.33
	DLD	9685	3.70	0.42	0.88	0.21	11.91	7.91	2.23	0.38	0.67	0.69	17.18	6.13
C	LB	292	3.91	0.35	1.49	0.35	6.50	3.30	2.81	0.23	9.28	5.56	35.88	3.59
	HS	100	3.85	0.67	1.71	0.84	6.33	4.33	2.95	0.30	12.55	13.75	37.32	6.64
	TL	159	3.54	0.59	1.87	0.74	5.21	4.97	2.72	0.30	9.48	6.91	37.96	5.21
	SD	219	3.91	0.37	1.54	0.47	6.61	4.68	2.85	0.19	10.75	7.68	36.24	5.02

	BLG	198	3.91	0.74	1.64	0.97	8.00	7.37	3.00	0.27	10.57	15.49	36.29	6.75
	DLD	203	3.94	0.48	1.50	0.43	6.96	5.24	2.87	0.27	9.41	6.04	35.89	4.27
T	LB	787	3.76	0.39	1.15	0.21	8.37	4.35	2.47	0.31	2.16	1.25	26.42	3.89
	HS	541	3.89	0.49	1.05	0.29	8.98	6.74	2.59	0.33	1.81	1.15	24.79	3.89
	TL	465	3.77	0.70	1.22	0.49	8.81	6.91	2.56	0.44	2.30	1.21	27.10	4.39
	SD	819	3.87	0.41	1.12	0.26	8.23	5.46	2.59	0.28	2.28	1.18	26.59	4.04
	BLG	665	4.04	0.51	1.04	0.31	10.33	7.31	2.72	0.33	2.19	1.13	25.66	4.44
	DLD	503	3.95	0.46	1.10	0.30	8.69	6.16	2.67	0.31	2.35	1.17	26.60	4.20
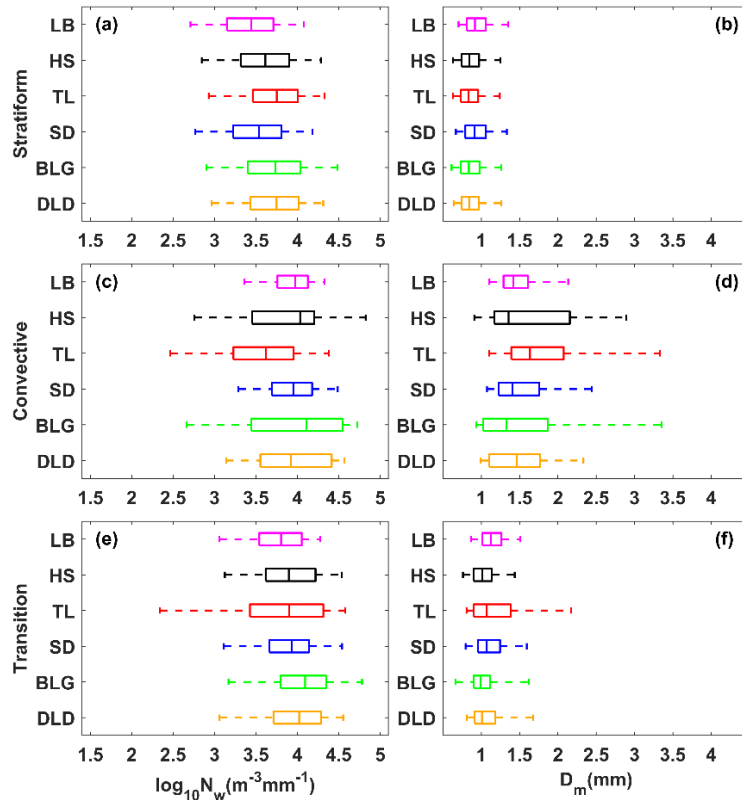
Figure 9. As in Fig. 5 but for different rain types at six sites.

3.5 Implications for radar rainfall estimation with DSD

The sixth moment of raindrop diameter is proportional to the radar reflectivity factor and the 3.76th moment is approximately the rain rate (they can be calculated by Equations 4 and 5). Generally, the theoretical basis of QPE for single polarization radar (ground-based or space-based) is the power relationship between the radar reflectivity and rainfall rate ($Z=AR^b$). This makes the coefficients A and exponents b of the power relationship heavily dependent on the variation in DSD. Therefore, it is necessary to obtain the A and b of different sites according to different rainfall types.

Figure 10 shows the Z-R scatter plots for different sites and the fitted power-law relationships for different rainfall types. The blue and red scatter points represent stratiform and convective rainfall, respectively. The purple, red and black solid lines indicate the Z-R relationships for stratiform, convective and total rainfall, respectively. It shows that the Z-R scatter points for HS and BLG were relatively scattered around the 5 mm h^{-1} rain rate. Besides, the Z-R relationship of total rainfall underestimated the

stratiform rainfall at low R values and the convective rainfall at high *R* values. Based on the average *Z-R* relationship using a least-squares method, the dispersion degree of *A* and *b* at different sites was 42.5% and 10.7%, respectively, which reveals there to be large differences in mountain areas.
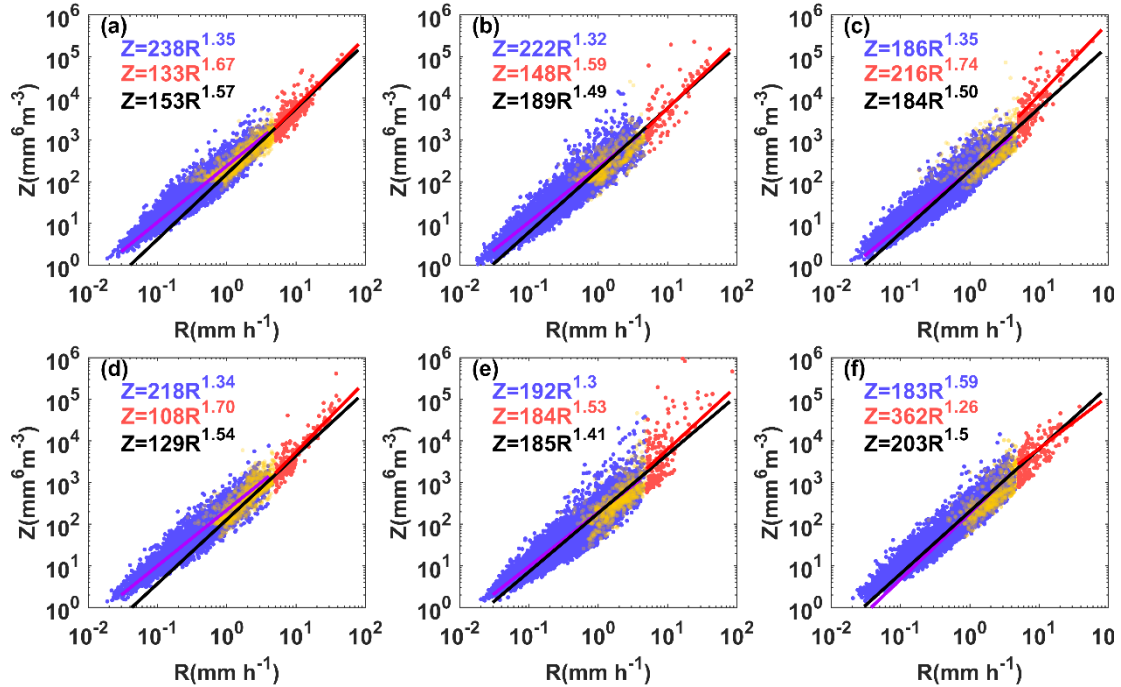
Figure 10. Scatter plots of Z ($mm^6\,m^{-3}$) versus R ($mm\,h^{-1}$) for three rain types at (a) LB, (b) HS, (c) TL, (d)SD, (e)BLG, and (f)DLD. The blue, red and yellow scatter points, represent stratiform, convective and transitional cases, respectively. The purple, red and black lines denote the *Z-R* relations. The blue, red and black formula denote stratiform, convective and total *Z-R* relationships.

In order to compare the six sites *Z-R* relationships with some standard *Z-R* relationships, the results for *Z=300R$^{1.4}$* for convective rainfall commonly used in radar, and *Z=200R$^{1.6}$* (i.e., M48) for stratiform rainfall commonly used in midlatitude areas, are provided in Figure 11. Overall, convective rainfall had smaller values of *A* and larger values of *b* than those of stratiform rainfall (excluding DLD). The *A* values of convective rainfall were smaller than the commonly used *Z-R* relationship with large differences, but the *b* values were greater. The distribution of *A* and *b* for stratiform rainfall was relatively concentrated, with *A* and *b* ranging from 186–238 and 1.3–1.35, respectively. The *A* values of SR were close to those of M48, and the *b* values were close to and smaller than the *Z-R* of global SR. Station DLD had a similar *Z-R* for stratiform rainfall with as M48, while its convective rainfall was different from other sites, with a larger A value (twice as large as other sites) and smaller *b* value. In addition, it is clear that the *A* value of stratiform rainfall increased from the southern slopes to northern slopes, while the opposite was the case for convective rainfall. Also, the *Z-R* relationships of the same section are more consistent, such as those of the interior or the northern slopes, which have distinct geographic characteristics.
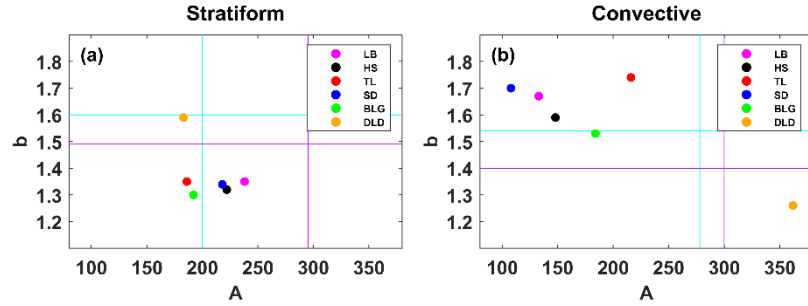
Figure 11. The *A* and *b* values of the *Z-R* relationships for (a) stratiform rainfall and (b) convective rainfall at six sites. The purple lines in (a) and cyan lines in (b) correspond to the global *Z-R* model ($Z = 295R^{1.49}$ for continental stratiform rainfall and $Z = 278R^{1.54}$ for convective rainfall, respectively) (Ghada et al., 2018). The cyan lines in (a) represent the midlatitude stratiform rainfall *Z-R* model ($Z = 200R^{1.60}$, Marshall, 1948); and the purple lines in (b) represent the convective rainfall *Z-R* model ($Z = 300R^{1.40}$) applied to operational weather radar (Fulton et al., 1998).

4 Discussion

The paper analyses the statistical characteristics of DSD at different sites in the Qilian Mountains during the rainy season, which not only contain rainfall classes and rainfall types but more importantly reflect the differences between different sites. The results from different aspects can be mutually confirmed and have a good representation of the spatial distribution, serving as a strong factual basis for discussion of the microphysical structure of precipitation. For example, with the rain rate class rising, the number concentration of all size bins is increased and the width of DSDs became wider, which manifested as convective rainfall having a larger rain rate. In spatial terms, the characteristics of precipitation in the interior of the mountains and on the southern slopes were closer, whether considering the overall DSD distribution or the distributions of DSD parameters. However, there were obvious variabilities at the interior sites for DSD parameters due to the influences of local dynamics and thermal effects. On the other hand, these characteristics also exhibited some differences between the interior and eastern sections of the Qilian Mountains, especially in the discussion of DSD parameters for rainfall classes and rainfall types (s Figures 5 and 9). This spatial variation in DSD suggests that microphysical processes involved in the DSD are influenced by complex topography (altitude, mountain alignment) and potentially related to the source of water vapor, development of precipitation process and anthropogenic factors.

Compared to previous studies that focused on eastern, southern and northern China as well the Tibetan Plateau, the Qilian Mountains region has its own unique DSD characteristics and Z-R relationship during the rainy season, including a smaller raindrop diameter with a higher number concentration. Moreover, the division of rainfall rate classes in the Qilian Mountains more adequately reflects the DSD characteristics in each class, unlike when using the classification method of other sites with larger rainfall rates. More importantly, the proposed classification of stratiform and convective rainfall can clearly distinguish between the distribution of $\log_{10}N_w$

versus D_m in different rainfall types, for which the dividing line (slope of −1.6 and intercept of 6.008) between stratiform and convective rainfall has the same slope as the line (slope of −1.6 and intercept of 6.3) given by Bringi et al (2003). Furthermore, according to this method, it can be easily proven that convective events are more consistent with the continental-like cluster, conforming to the precipitation characteristics of the Qilian Mountains .

As mentioned above, the characteristics of DSD mainly describe diameters larger than 0.2 mm, which is limited by the observation instruments being unable to detect small drops of diameter less than 0.2 mm. Therefor, it is not a complete DSD, and the number concentration of small drops of diameter less than 0.5 mm is underestimated. Recent studies have been devoted to improving DSD observations in order to overcome the limitations of disdrometers. A study by Thurai et al. (2017) obtained a more complete DSD by splicing 2DVD and MPS (Meteorological Particle Spectrometer) measurements to observe DSDs and developed a technology to reconstruct the drizzle-mode DSD (Raupach et al., 2019), whicha good presentation of the DSD of small raindrops was provided, and important applications were highlighted.

5 Summary and conclusion

Based on six months of DSD data observed over the southern slopes, northern slopes and interior of the Qilian Mountains, the characteristics and differences of DSD were studied, and the Z-R relationships of six sites were discussed. The main conclusions can be summarized as follows:

1. For all rainfall events, the number concentrations of small and large raindrops in the interior and on the southern slopes were greater than that on the northern slopes, while midsize raindrops were less. The DSD of the interior of the mountains showed great variability, mainly in terms of the $\log_{10}N_w$ and D_m (DSD parameters), which was quite different to the case for the northern slopes.

2. The rainfall rates were divided into six categories based on the DSD characteristics: C1, R<0.5; C2, 0.5≤R<2; C3, 2≤R<4; C4, 4≤R<6; C5, 6≤R<10; and C6, >10 mm h^{-1}. As the rainfall rate increased, the differences in number concentration of each raindrop size became significantly larger, especially at the interior sites. Besides, classes C5 and C6 made a relatively large contribution to the northern slopes, with a greater probability of heavy precipitation events.

3. The dispersion degree of $\log_{10}N_w$ and D_m at the six sites was 8.3% and 10.0% for stratiform rainfall and 10.4% and 23.4% for convective rainfall, respectively. It is easier to increase the number concentration of large raindrops in the interior area of the mountains during convective rainfall. Meanwhile, there is a greater increase in the number concentration of raindrops over the northern slopes during convective rainfall.

4. The dispersion degree of coefficient A and exponent b in the Z-R relationship for the six sites was 42.5% and 10.7%, respectively. Overall, the Z-R relationships of the ipsilateral sites were more consistent; and the A value of stratiform rainfall increased from the southern slopes to northern slopes, while the opposite was true

for convective rainfall. The *Z-R* relationships in stratiform rainfall were similar and generally underestimated by the *Z=200R^{1.6}* model used for midlatitude stratiform rainfall; and the *Z-R* relationships for convective precipitation varvaried greatly at different stations, which were overestimated by *Z=300R^{1.4}* at lower rain rates values and underestimated at higher rain rates values.

This study reveals the microphysical variability of precipitation over the complex topography of the arid and semi-arid regions of Northwest China, which can not only improve local numerical simulations, but also provides a basis for further understanding the differences in DSD characteristics formed at the mesoscale due to topographic factors and the water vapor distribution, etc. This study holds importance as a basis for the future implementation of weather modification techniques, which is of great significance in solving the shortage of water resources in the arid and semi-arid regions.

Data availability. Disdrometer data used in this study are available by contacting the authors.

Author contributions. WM conducted the detailed analysis; WZ provided financial support and conceived the idea; MK collated the observation data; all the authors contributed to the writing and revisions.

Competing interests. The authors declare that they have no conflict of interest.

Acknowledgments

The work was supported by Weather modification ability construction project of Northwest China under grant No. ZQC-R18208 and The Second Tibetan Plateau Comprehensive Scientific Expedition Grant No. 2019QZKK0104. Thanks are given to Asi Zhang for her help in discussing some questions. The authors also thank reviewers and editors for their helpful suggestion for this study

References

Adirosi, E., N. Roberto, M. Montopoli, E. Gorgucci, and L. Baldini, 2018: Influence of disdrometer type on weather radar algorithms from measured DSD: Application to Italian climatology. Atmosphere, 9, 360.

Angulo-Martínez, M., and A. Barros, 2015: Measurement uncertainty in rainfall kinetic energy and intensity relationships for soil erosion studies: An evaluation using PARSIVEL disdrometers in the Southern Appalachian Mountains. Geomorphology, 228, 28-40.

Atlas, D., R. Srivastava, and R. S. Sekhon, 1973: Doppler radar characteristics of precipitation at vertical incidence. Reviews of Geophysics, 11, 1-35.

Bringi, V., V. Chandrasekar, J. Hubbert, E. Gorgucci, W. Randeu, and M. Schoenhuber, 2003: Raindrop size distribution in different climatic regimes from disdrometer and dual-polarized radar analysis. Journal of the atmospheric sciences, 60, 354-365.

Campos, E., I. Zawadzki, M. Petitdidier, and W. Fernandez, 2006: Measurement of raindrop size distributions in tropical rain at Costa Rica. Journal of Hydrology, 328, 98-109.

Chen, B., J. Yang, and J. Pu, 2013: Statistical characteristics of raindrop size distribution in the Meiyu season observed in eastern China. Journal of the Meteorological Society of Japan. Ser. II, 91, 215-227.

Dolan, B., B. Fuchs, S. Rutledge, E. Barnes, and E. Thompson, 2018: Primary modes of global drop size distributions. Journal of the Atmospheric Sciences, 75, 1453-1476.

Das, S., and A. Maitra, 2018: Characterization of tropical precipitation using drop size distribution and rain rate-radar reflectivity relation. Theoretical and applied climatology, 132, 275-286.

Fu, Z., and Coauthors, 2020: Statistical characteristics of raindrop size distributions and parameters in Central China during the Meiyu seasons. Journal of Geophysical Research: Atmospheres, 125, e2019JD031954.

Fulton, R. A., J. P. Breidenbach, D.-J. Seo, D. A. Miller, and T. O'Bannon, 1998: The WSR-88D rainfall algorithm. Weather and forecasting, 13, 377-395.

Geoffroy, O., A. Siebesma, and F. Burnet, 2014: Characteristics of the raindrop distributions in RICO shallow cumulus. Atmospheric Chemistry and Physics, 14, 10897-10909.

Ghada, W., A. Buras, M. Lüpke, C. Schunk, and A. Menzel, 2018: Rain microstructure parameters vary with large-scale weather conditions in Lausanne, Switzerland. Remote Sensing, 10, 811.

Giannetti, F., and Coauthors, 2017: Real-time rain rate evaluation via satellite downlink signal attenuation measurement. Sensors, 17, 1864.

Gou, X., F. Chen, M. Yang, J. Li, J. Peng, and L. Jin, 2005: Climatic response of thick leaf spruce (Picea crassifolia) tree-ring width at different elevations over Qilian Mountains, northwestern China. Journal of Arid Environments, 61, 513-524.

609 Guyot, A., Pudashine, J., Protat, A., Uijlenhoet, R., Pauwels, V., Seed, A., and Walker,
610   J. P., 2019: Effect of disdrometer type on rain drop size distribution
611   characterisation: A new dataset for south-eastern Australia. Hydrology and Earth
612   System Sciences, 23, 4737-4761.
613 Jash, D., E. Resmi, C. Unnikrishnan, R. Sumesh, T. Sreekanth, N. Sukumar, and K.
614   Ramachandran, 2019: Variation in rain drop size distribution and rain integral
615   parameters during southwest monsoon over a tropical station: An inter-comparison
616   of disdrometer and Micro Rain Radar. Atmospheric Research, 217, 24-36.
617 Jaffrain, J., and Berne, A., 2011: Experimental quantification of the sampling
618   uncertainty associated with measurements from PARSIVEL disdrometers. Journal
619   of Hydrometeorology, 12, 352-370.
620 Kruger, A., and W. F. Krajewski, 2002: Two-dimensional video disdrometer: A
621   description. Journal of Atmospheric and Oceanic Technology, 19, 602-617.
622 Le Loh, J., D.-I. Lee, and C.-H. You, 2019: Inter-comparison of DSDs between
623   Jincheon and Miryang at South Korea. Atmospheric Research, 227, 52-65.
624 Li, Z., and Coauthors, 2019: Climate background, relative rate, and runoff effect of
625   multiphase water transformation in Qilian Mountains, the third pole region.
626   Science of The Total Environment, 663, 315-328.
627 Lim, Y. S., J. K. Kim, J. W. Kim, B. I. Park, and M. S. Kim, 2015: Analysis of the
628   relationship between the kinetic energy and intensity of rainfall in Daejeon, Korea.
629   Quaternary International, 384, 107-117.
630 Ma, L., L. Zhao, D. Yang, Y. Xiao, L. Zhang, and Y. Qiao, 2019a: Analysis of Raindrop
631   Size Distribution Characteristics in Permafrost Regions of the Qinghai–Tibet
632   Plateau Based on New Quality Control Scheme. Water, 11, 2265.
633 Ma, Y., G. Ni, C. V. Chandra, F. Tian, and H. Chen, 2019b: Statistical characteristics of
634   raindrop size distribution during rainy seasons in the Beijing urban area and
635   implications for radar rainfall estimation. Hydrology and Earth System Sciences,
636   23, 4153-4170.
637 Marshall, J. S., 1948: The distribution of raindrops with size. J. meteor., 5, 165-166.
638 McFarquhar, G. M., T.-L. Hsieh, M. Freer, J. Mascio, and B. F. Jewett, 2015: The
639   characterization of ice hydrometeor gamma size distributions as volumes in N0–
640   λ–μ phase space: Implications for microphysical process modeling. Journal of
641   Atmospheric Sciences, 72, 892-909.
642 Narayana Rao, T., N. Kirankumar, B. Radhakrishna, and D. Narayana Rao, 2006: On
643   the variability of the shape-slope parameter relations of the gamma raindrop size
644   distribution model. Geophysical research letters, 33.
645 Protat, A., and Coauthors, 2019: The latitudinal variability of oceanic rainfall properties
646   and its implication for satellite retrievals: 1. Drop size distribution properties.
647   Journal of Geophysical Research: Atmospheres, 124, 13291-13311.
648 Pu, K., X. Liu, Y. Wu, S. Hu, L. Liu, and T. Gao, 2020: A comparison study
649   of raindrop size distribution among five sites at the urban scale during the
650   East Asian rainy season. Journal of Hydrology, 590, 125500, https://doi.or

651   g/10.1016/j.jhydrol.2020.125500.

652 Penide, G., A. Protat, V. V. Kumar, and P. T. May, 2013: Comparison of two
653   convective/stratiform precipitation classification techniques: Radar reflectivity
654   texture versus drop size distribution–based approach. Journal of Atmospheric and
655   Oceanic Technology, 30, 2788-2797.

656 Qin, Y., H. Lei, D. Yang, B. Gao, Y. Wang, Z. Cong, and W. Fan, 2016: Long-term
657   change in the depth of seasonally frozen ground and its ecohydrological impacts
658   in the Qilian Mountains, northeastern Tibetan Plateau. Journal of Hydrology, 542,
659   204-221.

660 Rincon, R. F., and R. H. Lang, 2002: Microwave link dual-wavelength measurements
661   of path-average attenuation for the estimation of drop size distributions and rainfall.
662   IEEE Transactions on geoscience and remote sensing, 40, 760-770.

663 Raupach, T. H., M. Thurai, V. Bringi, and A. Berne, 2019: Reconstructing the drizzle
664   mode of the raindrop size distribution using double-moment normalization.
665   Journal of Applied Meteorology and Climatology, 58, 145-164.

666 Seela, B. K., J. Janapati, P. L. Lin, K. K. Reddy, R. Shirooka, and P. K. Wang, 2017: A
667   comparison study of summer season raindrop size distribution between Palau and
668   Taiwan, two islands in western Pacific. Journal of Geophysical Research:
669   Atmospheres, 122, 11,787-711,805.

670 Smith, J. A., E. Hui, M. Steiner, M. L. Baeck, W. F. Krajewski, and A. A. Ntelekos,
671   2009: Variability of rainfall rate and raindrop size distributions in heavy rain.
672   Water Resources Research, 45.

673 Thurai, M., P. Gatlin, and V. Bringi, 2016: Separating stratiform and convective rain
674   types based on the drop size distribution characteristics using 2D video
675   disdrometer data. Atmospheric Research, 169, 416-423.

676 Thurai, M., P. Gatlin, V. Bringi, W. Petersen, P. Kennedy, B. Notaroš, and L. Carey,
677   2017: Toward completing the raindrop size spectrum: Case studies involving 2D-
678   video disdrometer, droplet spectrometer, and polarimetric radar measurements.
679   Journal of Applied Meteorology and Climatology, 56, 877-896.

680 Testud, J., S. Oury, R. A. Black, P. Amayenc, and X. Dou, 2001: The concept of
681   "normalized" distribution to describe raindrop spectra: A tool for cloud physics
682   and cloud remote sensing. Journal of Applied Meteorology, 40, 1118-1140.

683 Tian, H., T. Yang, and Q. Liu, 2014: Climate change and glacier area shrinkage in the
684   Qilian mountains, China, from 1956 to 2010. Annals of Glaciology, 55, 187-197.

685 Ulbrich C W., 1983: Natural variations in the analytical form of the raindrop size
686   distribution. Journal of climate and applied meteorology, 22, 1764-1775.

687 Wainwright, C. E., D. T. Dawson, M. Xue, and G. Zhang, 2014: Diagnosing the
688   intercept parameters of the exponential drop size distributions in a single-moment
689   microphysics scheme and impact on supercell storm simulations. Journal of
690   Applied Meteorology and Climatology, 53, 2072-2090.

691 Wang, Y., J. Zheng, Z. Cheng, and B. Wang, 2020: Characteristics of Raindrop Size
692   Distribution on the Eastern Slope of the Tibetan Plateau in Summer. Atmosphere,

693   11, 562.

694 Wu, Y., and L. Liu, 2017: Statistical characteristics of raindrop size distribution in the
695   Tibetan Plateau and southern China. Advances in Atmospheric Sciences, 34, 727-
696   736.

697 Yang, L., J. Smith, M. L. Baeck, B. Smith, F. Tian, and D. Niyogi, 2016: Structure and
698   evolution of flash flood producing storms in a small urban watershed. Journal of
699   Geophysical Research: Atmospheres, 121, 3139-3152.

700 Zhang, A., and Coauthors, 2019: Statistical characteristics of raindrop size distribution
701   in the monsoon season observed in southern China. Remote Sensing, 11, 432.

702 Zhao, P., and Coauthors, 2019: The Tibetan Plateau surface-atmosphere coupling
703   system and its weather and climate effects: The Third Tibetan Plateau Atmospheric
704   Science Experiment. Journal of Meteorological Research, 33, 375-399.

705 Zeng, Y., and Coauthors, 2021: Statistical Characteristics of Raindrop Size Distribution
706   during Rainy Seasons in Northwest China. Advances in Meteorology, 2021.

707